Numerical and experimental investigation of the lift force on single bubbles

W. Dijkhuizen, M. van Sint Annaland *, J.A.M. Kuipers

Institute of Mechanics, Processes and Control Twente, Faculty of Science and Technology, University of Twente, P.O. Box 217, NL-7500 AE Enschede, The Netherlands

A B S T R A C T

In recent years CFD has proven itself as a valuable tool for gaining insight in flow phenomena in general and complex multiphase flows arising in process equipment in particular. However for (dispersed) multiphase flows, the reliability of the outcome of these computations depends in a sensitive way on the correctness of the representation of the phase interactions (for instance due to drag and lift forces) which leads to the well-known and difficult closure problem. In this paper we report results of direct numerical simulations supplemented with dedicated experiments to obtain quantitative data for the representation of the lift force. This force is known to be responsible for the segregation of small and large (deformed) bubbles in bubbly flows through pipes and bubble columns.

Both numerical simulations using an improved front tracking (FT) model and experiments under well-defined conditions have been performed for air bubbles rising through water/glycerine mixtures, where the bubble diameter, liquid viscosity and linear shear rate were varied. The numerical simulations show a good agreement with the correlation presented by Legendre and Magnaudet (1998) for spherical bubbles at sufficiently high Reynolds numbers. For large deformed bubbles a good agreement with the correlation by Tomiyama et al. (2002) was found over a wide range of liquid viscosities, although the computed lift force was always slightly lower. Therefore a new correlation has been proposed, which combines a fit of the numerical data for deformed bubbles with the correlation by Legendre and Magnaudet (1998) for small bubbles. Finally, it was shown that the shear rate has no significant influence on the drag and lift coefficient.

An experimental set-up (similar to the one used by Tomiyama) was constructed using a running belt submerged in a liquid, consisting of a glycerine–water mixture of varying viscosity. PIV measurements have been used to calibrate the linear shear field and to obtain the flow profile around the bubbles. Contrary to the numerical simulations, the experimental data show a very strong influence of the shear rate on the lift force coefficient. This may be attributed to the rigid behaviour of the contaminated bubble surface, which changes the shear stress at the bubble interface.

1. Introduction

1.1. Modeling of gas–liquid flows

Multiphase systems are widely encountered in industrial processes, involving a.o. metal casting, fuel synthesis (Fischer-Tropsch), slurry polymerization and oil processing. The hydrodynamics of these systems are poorly understood and are dictated by the complex interactions between the phases. In order to resolve all different time-scales and length-scales, a multi-level modeling strategy is used (van Sint Annaland et al., 2003), based on three different models with differing degree of sophistication. At the lowest (most detailed) level, direct numerical simulation (DNS) is used to predict the bubble shape, as well as the flow field inside and outside the bubble by solving the Navier–Stokes on a sufficiently refined computational mesh. The DNS results can be used to obtain closures for the forces acting on a single or a few bubbles or droplets, such as the drag, lift and virtual mass forces.

One level higher, the discrete bubble model (DBM) is used to handle systems with a large number of bubbles ($< O(10^6)$), at the expense of information about the bubble shape and the detailed flow field in the vicinity of individual bubbles. Therefore, this information has to be supplied in the form of closures for the forces acting on the bubbles, which also implicitly contains the bubble shape.

Finally, industrial systems are mainly modelled using an Euler–Euler approach, which does not even discriminate between individual bubbles on a sub-grid scale. However, the same closures can be used as for the DBM, supplemented by bubble population balances to account for coalescence and break-up of the bubbles.

1.2. Interfacial closures

Closures for forces acting on dispersed elements can be obtained from analytical theory, dedicated experiments and

* Corresponding author. Tel.: +31 53 4894478; fax: +31 53 4892882.
 E-mail address: M.vanSintAnnaland@utwente.nl (M. van Sint Annaland).

DNS, each with their own strong and weak points. Analytical theory is often limited to idealized situations, for instance spherical bubbles rising in viscous liquids, which differ largely from industrially relevant cases, where bubbles are usually deformed and the flow pattern can be very dynamic. Nevertheless, analytical theory is invaluable when it comes to validation of experiments and numerical simulations (in limiting cases).

On the other hand experiments often suffer from factors which are difficult to control such as the effect of contaminants (Clift et al., 1978), which increase the drag force by changing the slip condition at the surface from no-shear to no-slip (Fig. 1). Secondly, a gradient in the concentration of contaminants present at the bubble surface can create a Marangoni convection pattern opposing to the direction of motion (Palaparthi et al., 2005). The difficulty for experiments lies in determination of how pure the system is, and how the physical properties are altered by a small amount of contaminants. In addition it may be very difficult to experimentally determine all the required information simultaneously and non-invasively, as for example for the drag force acting on bubbles rising in a dense swarm.

DNS can be used to overcome some of the problems faced by analytical theory and experiments, since it is not limited to idealized systems and contaminants are not an issue, which however can also be regarded as a drawback. Moreover, it is very easy to change physical properties and other parameters, allowing for extensive parameter studies that are not practical or difficult to perform by means of experiments.

1.3. Direct numerical simulations

There are many different DNS models available in literature for multiphase flows with deformable interfaces. For a more thorough overview the interested reader is referred to van Sint Annaland et al. (2006). The main difference between these models is in the description of the phase boundaries: while the volume of fluid (VOF) and lattice Boltzmann (LB) models both capture the interface using data from the fixed grid, the front tracking (FT) model tracks the interface explicitly using a Lagrangian surface mesh. As a consequence, the LB and VOF models exhibit automatic-potentially unphysical-coalescence when two bubbles meet, since the model cannot distinguish them at a length scale smaller than the size of the computational grid. On the other hand the FT model needs a sub grid model to allow bubbles to merge (Singh and Shyy, 2007). This difference makes FT uniquely qualified for studying gas bubbles behaviour in dense swarms. Secondly, the superior interface resolution of the FT model is potentially more accurate for the description of surface tension effects. 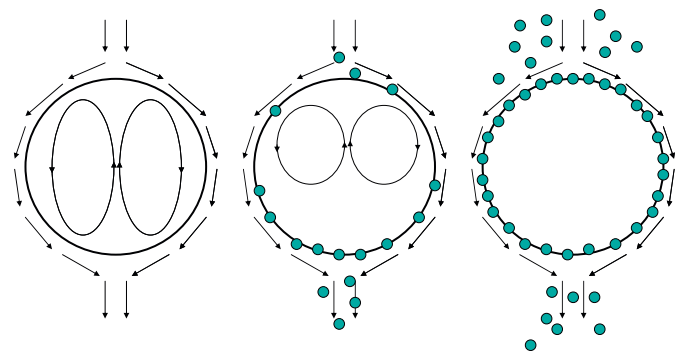Of course FT also has some drawbacks, most notably the fact that the volume of the dispersed phases is not intrinsically conserved. Also the need for restructuring of the front is generally regarded as a drawback in literature.

The main challenges for DNS are related to the treatment of the surface tension, large density jumps at the interface and high Reynolds numbers, which can all be found in the important air/water system. A high surface tension (small bubbles) causes unphysical velocity vectors, which may lead to excessive volume loss or other instabilities. As an illustration, standard FT is unable to simulate a 1 mm air bubble rising in water, since it vanishes due to volume losses of the dispersed phase before it has reached its steady-state rise velocity. While other DNS models do conserve the bubble volume, they are usually plagued by even greater numerical stability problems, making it extremely difficult to carry out these simulations. As a consequence Scardovelli and Zaleski (1999) and Zaleski (2005) concluded that there is no three-dimensional calculation of a falling drop or rising bubble in the difficult air/water conditions.

1.4. Objectives

In this article, an improved 3D front tracking model is used to study the lift force, which is responsible for segregation of small and large bubbles in bubbly flows through pipes and bubble columns: small spherical bubbles move to the wall, while large deformed bubbles move towards the core region (Fig. 2). It has been demonstrated numerically for pure spherical bubbles (Legendre and Magnaudet, 1998) that at low Reynolds numbers the lift force results from both viscous and pressure effects, while at high Reynolds numbers, the pressure effect dominates. In either case the lift force coefficient is always positive for pure spherical bubbles. On the other hand, for (larger) deformed bubbles it has been established both experimentally (Tomiyama et al., 2002) and numerically (Adoua et al., 2009) that the sign of the lift force coefficient becomes negative.

Secondly, experiments are included to highlight the effect of contaminations on the lift force. Recently, Fukuta et al. (2008) showed that for a spherical contaminated bubble ($Re=100$, $Sr=0.2$) the lift force can become negative. This is also in line with what is known for a rotating rigid sphere (Kurose and Kumori, 1999; Bagchi and Balachander, 2002).

In the following chapters, first the most important lift force correlations from literature are described and their applicability is discussed. Secondly, based on a force balance for a discrete bubble in a shear flow, equations are derived to obtain the drag and lift force coefficients. In the remainder of this article, the
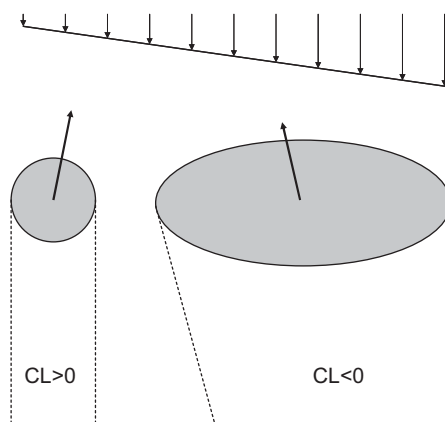

Fig. 1. Schematic overview of the effect of contaminants on the drag force. From left to right: ultrapure liquid with no-shear boundary condition at the bubble interface; slightly contaminated liquid with a limited circulation inside the bubble; fully contaminated bubble, without any circulation (full no-slip boundary).

Fig. 2. Two limiting cases of the lift force: small spherical bubbles move to the high negative velocity side, while large deformed bubbles move in the opposite direction.

experimental set-up and numerical aspects are described, followed by a combined description of the results.

2. Existing lift force closures

Equations for the lift force for the two limiting cases of low and high Reynolds numbers have been analytically derived for spherical bubbles. Saffman (1965) was the first to derive an expression for the lift force acting on a slowly rotating sphere in the limit of zero Reynolds number and infinite shear ratio (Sr). This result was extended to arbitrary shear rates by McLaughlin (1991), which allows it to be used for practical purposes (Eq. (1)). It can be seen that the lift coefficient at low Reynolds numbers is strongly dependant on both the Reynolds number (Re) as well as the shear ratio (Sr).

$$C_L = 1.37 \frac{J(Re, Sr)}{\sqrt{Re\, Sr}} \quad Re \ll 1 \tag{1}$$

$$Re = \frac{\rho |\mathbf{v} - \mathbf{u}| d}{\eta} \tag{2}$$

$$Sr = \frac{\omega d}{|\mathbf{v} - \mathbf{u}|} \tag{3}$$

Mei and Klausner (1994) showed—using the same methodology as McLaughlin—that the lift force for a bubble is simply 2/3rd of that of a rigid particle. Unfortunately, Legendre and Magnaudet (1997) found an error in their derivation and derived that the lift force coefficient for a bubble should be 4/9th of the rigid sphere solution:

$$C_L = \left(\frac{2}{3}\right)^2 C_{L,McLaughlin} = \frac{6}{\pi^2} \frac{J(Re, Sr)}{\sqrt{Re\, Sr}}$$

$$J(Re, Sr) = \frac{2.255}{\left(1 + 0.2\frac{Re}{Sr}\right)^{3/2}} \quad Re \ll 1 \tag{4}$$

At the high Reynolds limit, Auton (1987) showed that the lift coefficient of a spherical bubble or particle is equal to a constant value of 1/2. Legendre and Magnaudet (1998) bridged the gap between these two limiting analytical solutions (Eq. (5)) by simulating spherical bubbles in a weak linear shear field at Reynolds numbers between 0.1 and 500. Especially the low Reynolds limit proved to be very challenging, because of the strong influence of the size of the computational domain. Their empirical correlation reduces to the analytical solutions at both extremes and is valid for all Reynolds numbers.

$$C_L = \sqrt{\left(\frac{6J(Re, Sr)}{\pi^2 \sqrt{Re\, Sr}}\right)^2 + \left(\frac{1}{2}\frac{Re + 16}{Re + 29}\right)^2} \quad Sr \ll 1 \tag{5}$$

Results for the lift force on deformed bubbles on the other hand are relatively scarce, since the level of complexity increases substantially. Analytically, the analysis by Auton was extended to ellipsoidal bubbles moving along their minor axis by Naciri (1992), who found a positive lift coefficient, demonstrating that deformation by itself does not change the direction of the lift force. Recently, these results for ellipsoidal bubbles in the inviscid limit (high Re) were confirmed by Adoua et al. (2009) using numerical simulations, which fit the following correlation:

$$C_L = 0.5 + 0.612\left(\frac{1 - E}{E}\right) \quad Re \to \infty \tag{6}$$

More importantly however, they show that the lift force does become negative for bubbles with an aspect ratio (E) lower than 0.37–0.45, in an intermediate band of Reynolds numbers

($100 < Re < 2000$) and for sufficiently low dimensionless shear rates ($Sr < 0.1$). They attribute this effect to the vorticity generated at the bubble surface, which gives a system of two counter-rotating streamwise vortices with opposite sign to that induced by the classical inviscid tilting of the upstream vorticity around the bubble.

Experimentally, the most significant work has been carried out by Tomiyama et al. (2002), who used a linear shear field in viscous liquids ($10^{-5.5} < Mo < 10^{-2.8}$). The corresponding closure for the lift force (Eq. (7)) is based on a modified Eötvös number (Eq. (8)) and reduces to zero for very small bubbles. Hibiki and Ishii (2007) combined the experimental data by Tomiyama et al. with Eq. (5), aiming at extending the range of applicability of this correlation (Eq. (9)). Unfortunately, in their paper they have to conclude that there is no literature data available to test the validity at higher Reynolds numbers (i.e. air–water system).

$$C_L = \begin{cases} MIN(0.288\tanh(0.121Re), f(Eo_H)) & Eo_H < 4 \\ f(Eo_H) = 0.00105Eo_H^3 - 0.0159Eo_H^2 - 0.0204Eo_H + 0.474 & 4 \le Eo_H < 10.7 \end{cases} \tag{7}$$

$$Eo_H = \frac{(\rho_l - \rho_g)g d_H^2}{\sigma} \tag{8}$$

$$C_L = [2 - \exp(0.136Eo^{1.11})]\sqrt{\left(\frac{6J(Re, Sr)}{\pi^2 \sqrt{Re\, Sr}}\right)^2 + \left(\frac{1}{2}\frac{Re + 16}{Re + 29}\right)^2} \quad 3.68 \le Re \le 78.8 \tag{9}$$

Numerically, Bothe et al. (2006) obtained lift coefficients slightly lower than predicted by the correlation by Tomiyama, using similar viscous liquids. Secondly, they conclude by cubic extrapolation that the lift force coefficient at low Eötvös numbers approaches 0.5, which is the analytical solution for a spherical bubble at high Reynolds numbers. It would be interesting to see whether the lift coefficient also approaches 1/2 for the case of a much lower viscosity liquid (i.e. water). For more viscous liquids, there should be no limiting value for the lift coefficient, as it depends strongly on the Reynolds number (Eq. (5)).

3. Improved 3D front tracking model

Compared to other DNS techniques, front tracking (FT; Unverdi and Tryggvason, 1992) offers a potentially more accurate surface tension treatment, because of the sub-grid interface representation. In addition, the explicit interface tracking prevents unphysical coalescence of bubbles, which is particularly important when studying dense bubble swarms. However, FT also has some drawbacks, most notably the fact that the volume conservation of the dispersed phases is not intrinsically enforced. Also, the need for restructuring of the front is generally regarded as a drawback in literature.

In this article a standard 3D FT model (van Sint Annaland et al., 2006) has been improved, to allow the simulation of even very small bubbles, with very high surface tension, without numerical problems such as volume loss and spurious currents. More specifically, the following has been changed:

- Direct coupling between the surface tension and the pressure jump at the interface, to reduce the magnitude of spurious currents while maintaining a sharp interface representation.
- Direct calculation of the phase fractions from the interface triangulation, eliminating the standard, but computationally expensive and diffusive method proposed by Unverdi and Tryggvason (1992).
- Higher order advection of the interface, to reduce volume conservation errors and improve interface smoothness.

- Semi-implicit treatment of the stress tensor, avoiding time-step limitations for highly viscous flows.

In the following paragraphs a brief general description of the above mentioned features of the improved FT model is given. For more detailed information about the numerical method the user is referred to Dijkhuizen et al. (2009).

3.1. Governing equations

In the FT model the Navier–Stokes equations are solved together with the continuity equation for incompressible media:

$$\nabla \cdot \mathbf{u} = 0 \tag{10}$$

$$\frac{\partial}{\partial t}(\rho \mathbf{u}) + \nabla \cdot \rho \mathbf{u}\mathbf{u} = -\nabla p + \rho \mathbf{g} + \nabla \cdot \mu[(\nabla \mathbf{u}) + (\nabla \mathbf{u})^T] + \mathbf{F}_\sigma \tag{11}$$

where the density ρ and the viscosity μ are locally averaged over all the phases present, based on the phase fraction F_i. The surface tension is included as a volumetric force density $\mathbf{F}_\sigma$ acting only in the vicinity of the interface.

The Navier–Stokes equations are solved on a staggered Cartesian mesh with a finite volume technique using an implicit treatment of the pressure gradient and diffusion terms and an explicit treatment of the convection. For the convection term a second order flux delimited Barton scheme is used (Centrella and Wilson, 1984) and for the diffusion term a standard second order finite difference scheme is used. To be able to simulate large density ratios, the Navier–Stokes equations are rewritten in their non-conservative form using the continuity equation (Van Sint Annaland et al., 2003):

$$\rho\left[\frac{\partial \mathbf{u}}{\partial t} + \nabla \cdot \mathbf{u}\mathbf{u}\right] = -\nabla p + \rho \mathbf{g} + \nabla \cdot \mu[(\nabla \mathbf{u}) + (\nabla \mathbf{u})^T] + \mathbf{F}_\sigma \tag{12}$$

A three step projection-correction method is used to solve the two equations: first the velocity is estimated using the explicit terms in the Navier–Stokes equations. Secondly a robust ICCG method is used to solve for the implicit diffusion terms, so that the numerical timestep is not limited in viscous systems. Finally, we use the same ICCG solver for the pressure correction to satisfy the incompressibility constraint.

3.2. Average fluid properties

For the local density linear weighing of all the phase fractions is used:

$$\rho = \sum_{i=1}^{nphases} F_i \rho_i \tag{13}$$

where F_i represents the fraction of phase i. Usually the viscosity is also linearly averaged, but here a more fundamental approach is used based on harmonic averaging of the kinematic viscosities (Prosperetti, 2002):

$$\frac{\rho}{\mu} = \sum_{i=1}^{nphases} F_i \frac{\rho_i}{\mu_i} \tag{14}$$

3.3. Surface tension

Making direct use of the triangulation of the interface, the surface tension acting on marker m is calculated via a contour integral over the tensile forces (van Sint Annaland et al., 2003):

$$\mathbf{F}_{\sigma,m} = \frac{\sigma}{dx\,dy\,dz} \oint_l (\mathbf{t}_m \times \mathbf{n}_m)\,dl \tag{15}$$

where $\mathbf{t}_m$ is the counter clockwise unit tangent vector along the edges of the marker m and l is the length of these tangent vectors (the perimeter of the marker). This method avoids the computation of the numerically inaccurate curvature and can be used for surfaces with a very high curvature with less numerical instability and better accuracy. The surface tension is mapped on to the Eulerian grid using a summation over all the markers m and their

Table 1
Literature values for the maximum steady-state spurious currents around a perfect sphere.

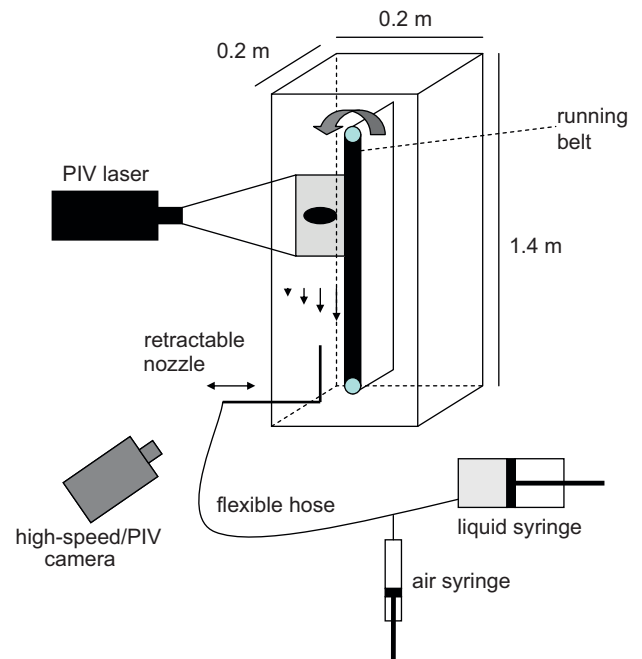| Source	$d/\Delta x$	La	Ca
de Sousa et al. (2004)	12.5	250	$O(10^{-3})$
	25		$O(10^{-4})$
Singh and Shyy (2007)	–	250–12000	$O(10^{-4})$
This work	≥ 10	1–10000	$< 2.2 \times 10^{-5}$

Fig. 3. Schematic overview of the experimental set-up.

Table 2
Equipment used for the high-speed imaging and PIV experiments.

Equipment	Details
Column	Polycarbonate walls, steel bottom section ($0.20 \times 0.20 \times 1.40$ m)
PIV laser	Double pulsed Nd-YAG laser New Wave Solo IV PIV 2 * 50 mJ@532 nm, f=50 Hz
Camera (both PIV and high-speed imaging)	Imager Pro HS CMOS camera 10 bits, 1280 * 1024 Pixels, Pixel size 12 * 12 µm Max. 625 frames/s, 50 mm camera lens Field-of-view: 0.068×0.108 m (w × h)
PIV tracer particles	Dantec 50 µm polyamide, 0.1%vol
Backlighting (high-speed imaging)	500 W halogen light and white 80 g paper covering the back wall of the column
Computer	Dual Xeon 2.66 GHz Programmable timing unit
PIV software	LaVision DaVis 7.1.1.44

edges l:

$$\mathbf{F}_\sigma = \frac{\sum_m\sum_l D(\mathbf{x} - \mathbf{x}_{m,l})\sigma(\mathbf{t}_{m,l} \times \mathbf{n}_{m,l})}{dx\,dy\,dz} \tag{16}$$

where $\mathbf{t}_{m,l}$ is the tangential vector and D is the distribution kernel, for which in this work density weighing (Deen et al., 2004) is used. Density weighing avoids mapping the surface tension force to a cell with a low mass, which can cause large distortions of the velocity field near the interface. Tryggvason et al. (2001) use a polynomial fit to obtain the normal and tangential vectors, but with our method the surface tension is calculated directly from the discrete triangulation.

3.4. Interfacial pressure jump

The coupling between surface tension and the pressure jump at the interface is crucially important to prevent unphysical
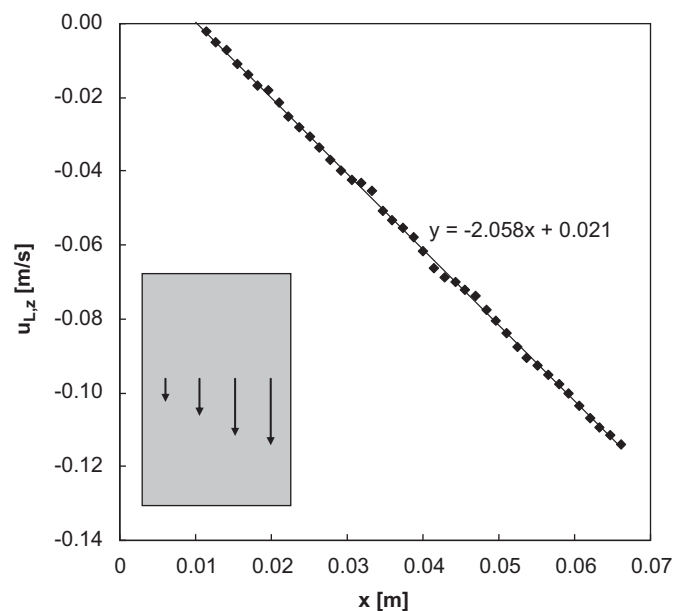

Fig. 4. Example of the linear shear field calibration. The dots represent the vertical component of the velocity in the middle of the camera view. A linear fit is used to obtain the shear rate and the position of the wall.

spurious currents, as was demonstrated by Popinet and Zaleski (1999) using a 2D front tracking model. They used a large computational stencil (3×3 nodes) to accurately capture the pressure jump at the interface. However, this is not feasible in 3D, due to the resulting computationally prohibitive 27-band pressure matrix. Moreover, it is important to understand that interfacial tension creates a pressure discontinuity at the position of the front, which is not easily accounted for in a Eulerian framework, even with higher order discretisations.

The magnitude of the pressure jump related to the surface tension can easily be calculated from the jump condition, when the shear stress in the normal direction is neglected (Eq. (17)). This makes it possible to separate the pressure inside the dispersed phases into a continuous (dynamic) part and a discontinuous pressure jump, which can be mapped to the Euler grid in the same way as the surface tension force. The main advantage is that now both the surface tension and the pressure jump act at exactly the same location, which means that only a relatively small net force will be transmitted to the Eulerian grid. This is much more accurate than a purely Eulerian treatment of the pressure discontinuity, thereby leading to much lower spurious currents (Table 1) and improved numerical stability. All of this is realized with hardly any additional computational cost, because the surface tension has already been calculated.

$$\int_{\partial S}[p]\,dS = \int_{\partial S}\mathbf{F}_\sigma \cdot \mathbf{n}\,dS$$

$$[p] = \frac{\int_{\partial S}\mathbf{F}_\sigma \cdot \mathbf{n}\,dS}{\int_{\partial S}dS} = \frac{\sum_m\mathbf{F}_{\sigma,m} \cdot \mathbf{n}_m S_m}{\sum_m S_m} \tag{17}$$

3.5. Calculation of the phase fractions

Traditionally, in the FT model the phase fractions are calculated by a method proposed by Unverdi and Tryggvason (1992):

$$\nabla^2 F = \nabla \cdot \mathbf{G}$$

$$\mathbf{G} = \sum_m D(\mathbf{x} - \mathbf{x}_m)\mathbf{n}_m \Delta s_m \tag{18}$$

where $\mathbf{n}_m$ is the outwards pointing normal and Δs_m is the surface area of the marker. First the gradient $\mathbf{G}$ is calculated from the interface markers, after which an ICCG method is used to solve this Poisson equation.

Table 3
Physical properties and stable linear shear rates for the water/glycerine mixtures used in the experiments and numerical simulations.

	Viscosity (mPa s)	Density (kg m^{-3})	Surface tension (mN m^{-1})	Morton number (Mo)	Experimental linear shear rates (s^{-1})
I	153	1228	65	1.57×10^{-2}	2.0, 4.0
II	81.8	1217	66	1.25×10^{-3}	1.5, 2.0, 3.0
III	45.7	1202	66	1.24×10^{-4}	1.5, 2.0
IV	25.4	1185	67	1.14×10^{-5}	1.0
V	12.3	1163	68	6.05×10^{-7}	
VI	5.04	1122	69	1.71×10^{-8}	
VII	2.23	1071	69	6.87×10^{-10}	
VIII	0.899	998	72	1.72×10^{-11}	

Table 4
Measurements devices used to obtain the physical properties of the water/glycerin mixtures.

Quantity	Measurement device	Error
Density	PAAR DMA 58	0.1 kg m^{-3}
Viscosity	Tamson thermostatic bath. Ubbelohde viscometers 65280 (I, II), 68145 (III, IV), 67365 (V, VI) and 6401 (VII, VIII).	1%
Surface tension	KRÜSS K9 with platinum plate	1 mN m^{-1}

It was found that this method smears out the phase fraction near the interface and it creates overshoots and undershoots of F, which have to be filtered out because of stability issues. To improve on this, our improved FT model uses a simple geometrical procedure to calculate the exact volume under the interface triangulation in each cell. This ensures that the phase fraction field remains sharp near the interface and also reduces volume losses. Finally, the computationally expensive iterative procedure to solve the Poisson equation (Eq. (18)) can be replaced by a simple explicit algorithm, which saves valuable computational time.

3.6. Updating the interface

Once the flow field has been found on the Eulerian grid, each marker point of the interface triangulation is moved with the local flow field. For the velocity interpolation to the marker points a 3rd order spline is used and the points are moved with a 4th order Runge–Kutta scheme. This combination of higher order methods ensures that the interface stays smooth and the volume error due to moving the mesh is negligible.

After some time the surface grid will become deformed. Some markers will become too large or too stretched, while others become too small. To maintain an adequate resolution, points will have to be added at some places and removed at other places. In this work a similar approach as described by Unverdi and Tryggvason (1992) is followed.

4. Experimental set-up

The experimental set-up consists of a square polycarbonate column with a steel bottom section containing a long thin tube, through which bubbles can be injected by means of a novel injection method using two syringes (Fig. 3). The first syringe has a needle and is used to inject a specific amount of air trough a membrane in a hose filled with liquid, after which the second syringe—filled with liquid—forces the bubble through the nozzle. Typically, the bubble is pushed through the injection tube at a rate of 0.01 m/s. It was found that this indirect injection technique enables a reproducible injection of the bubbles, allowing for a wide range of bubble diameters, without bubble break-up or excessive disturbances of the liquid in the column. Experiments with different water/glycerin mixtures were performed. A 15 cm wide running belt is suspended in the liquid to generate a linear shear field. A gap between the wall and the belt of 6 cm is used,
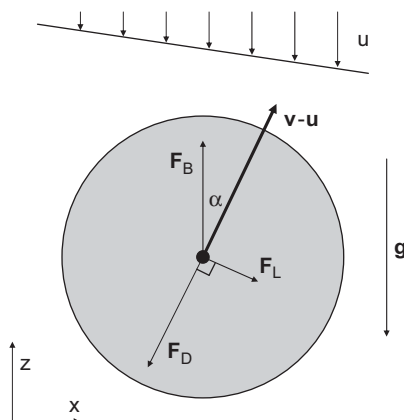
twice the distance used by Tomiyama et al. (2002), in order to reduce wall-effects. The direction of the belt is such that the bubbles experience counter flow, which helps to keep them in the field of view as long as possible.

For the measurement of the velocity field, a commercial PIV set-up is used, consisting of a double-pulsed Nd-YAG laser and high-speed camera (Table 2). Before each set of measurements, the linear shear field is calibrated using PIV. The velocity profile across the centre of the field of view (Fig. 4) was analyzed every 5 s for 35 s, which yields the shear rate and its standard deviation. From this the stable shear rates at different liquid viscosities are obtained (Table 3).

A high speed camera is used to track the motion of the bubbles at 100 Hz, using backlighting from a single 500 W halogen light. The back of the column is covered with white paper to give a diffuse lighting, thereby eliminating any reflections via the bubble surface or the column walls. The bubble dimensions and its centre
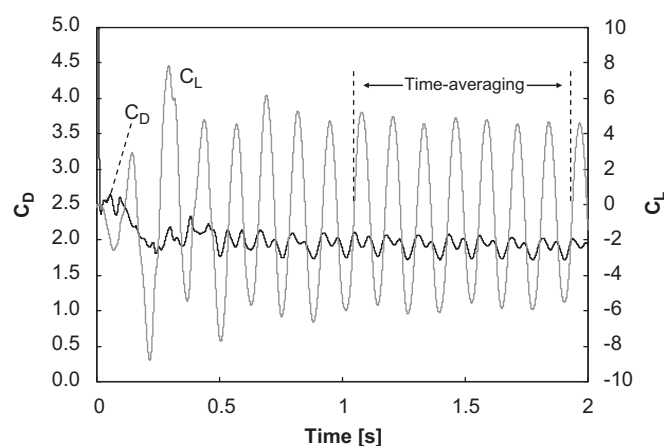

Fig. 6. Example of the time-averaging of the drag and lift forces for a simulated 8 mm air bubble in liquid VI.

Fig. 5. Force balance on a bubble rising in a linear shear field, indicating the direction of the buoyancy, lift and drag forces (in clockwise order). α represents the instantaneous angle between the direction of motion and the z-axis.
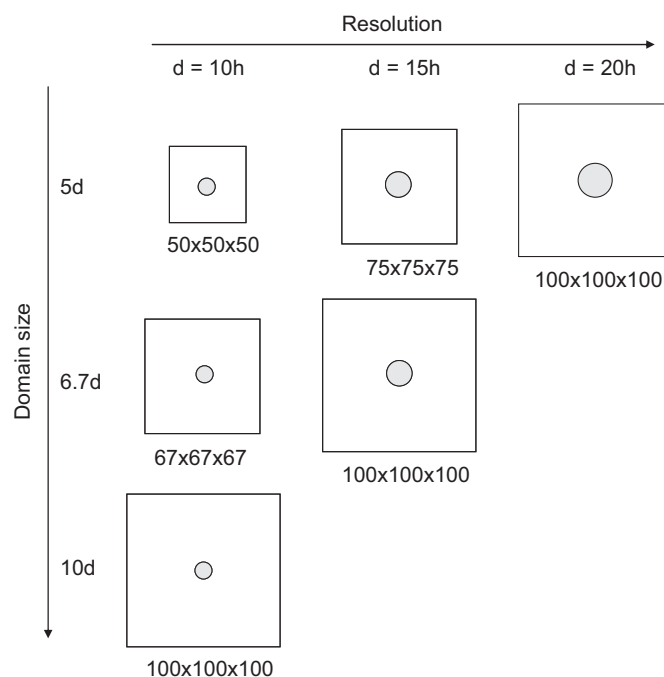

Fig. 7. Numerical simulation domains used for the lift force simulations, which are tuned to the viscosity of the liquid. Highly viscous liquids require a large domain (bottom left), while inviscid liquids require more interface resolution (top right).

of mass are determined at three points: after it enters, in the middle and before it leaves the field of view of the camera. Since the scale on the syringes used to inject air was not sufficiently accurate and there is an effect of the change in hydrostatic pressure as a function of the vertical position in the column, the equivalent bubble diameter is calculated from the measured horizontal and vertical bubble diameter:

$$d = (d_h^2 d_v)^{1/3} \tag{19}$$

The physical properties of the water/glycerine mixtures (Table 3) were measured at exactly the same temperature as was used in the experiments, using the same thermometer (0.1 °C accuracy). The measurement devices and settings used to obtain the physical properties are listed in Table 4. After each measurement series the glycerine was diluted with demineralized water to obtain a new liquid with a viscosity approximately two times lower.

5. Numerical simulations

The numerical simulations have been carried out with an improved FT model using a cubic computational domain consisting of typically one million cells, which yields good resolution at reasonable calculation time (typically two weeks on a single CPU). The initially spherical bubble is placed horizontally in the centre of the computational domain and a window shifting technique assures that it keeps this position. Depending on the viscosity of the liquid, the bubble diameter is equal to 15 or 20 Eulerian cells, which is the best trade-off between acceptable domain size and required resolution. The top, left and right boundaries enforce the linear shear field, using inflow and no-slip boundary conditions respectively. They are supplemented by a prescribed pressure boundary at the bottom, where the liquid is free to exit the domain, and free-slip boundaries at the front and rear. In the next paragraphs first of all an expression for the lift force coefficient will be derived, based on the bubble rise velocity which may oscillate due to shape and path instabilities. Secondly, the influence of the grid size and distance to the boundaries has been studied, showing that grid independent results can be obtained for sufficiently high Reynolds numbers. Finally, the influence of the numerical time step and initial conditions has been clarified.

5.1. Derivation of the force coefficients

The drag and lift coefficients for a bubble in a linear shear flow (Fig. 5) can be obtained from a steady-state force balance, including buoyancy ($\mathbf{F}_B$), drag ($\mathbf{F}_D$) and lift ($\mathbf{F}_L$) forces. A spherical-equivalent bubble diameter is used, so that the resulting closures can be applied without any additional equations, such as e.g. for the actual bubble shape. For bubbles experiencing path-instability, time-averaging is necessary to compute the drag and lift coefficients. The time-averaged forces are chosen as a basis, so that the time-averaged momentum exchange between the bubbles and the liquid phase is correct:

$$0 = \langle \mathbf{F}_B \rangle + \langle \mathbf{F}_D \rangle + \langle \mathbf{F}_L \rangle$$

$$0 = \frac{\pi}{6} d^3 (\rho_L - \rho_G) \mathbf{g} - \frac{\pi}{8} d^2 \rho_L C_D \langle \mathbf{v} - \mathbf{u} | (\mathbf{v} - \mathbf{u}) \rangle$$
$$- \frac{\pi}{6} d^3 \rho_L C_L \langle (\mathbf{v} - \mathbf{u}) \times (\nabla \times \mathbf{u}) \rangle \tag{20}$$

Because the drag and lift forces are perpendicular to each other, they can easily be separated. First of all, the drag coefficient

Table 5
Effect of the domain size and interface resolution on the drag and lift coefficient for a bubble in a linear shear field.

Liquid	d (mm)	Domain size	C_D			C_L		
			$d=10dx$	$d=15dx$	$d=20dx$	$d=10dx$	$d=15dx$	$d=20dx$
I	2	5d	54.5	55.0		−0.03	−0.24	
		6.7d	47.5	48.6		0.00	0.08	
		10d	42.6			0.59		
	6	5d	4.06	4.15		−0.41	−0.46	
		6.7d	3.84	3.92		−0.46	−0.50	
		10d	3.87			−0.45		
II	2	5d	18.14	17.80		0.40	0.43	
		6.7d	16.16	15.89		0.58	0.54	
		10d	15.06			0.58		
	6	5d	2.45	2.48		−0.21	−0.26	
		6.7d	2.35	2.37		−0.24	−0.28	
		10d	2.35			−0.18		
III	2	5d	7.20	6.82	6.76	0.36[*]	0.37	0.40
		6.7d	6.59	6.34		0.34[*]	0.36	
		10d	6.33			0.37[*]		
	6	5d	1.82	1.84	1.85	−0.24	−0.27	−0.29
		6.7d	1.74	1.77		−0.23	−0.28	
		10d	1.71			−0.25		
IV	2	5d	3.30	3.05	2.99	0.33[*]	0.33	0.33
		6.7d	3.12	2.92		0.29[*]	0.33	
		10d	3.08			0.26[*]		
	6	5d	1.48	1.52	1.54	−0.33	−0.37	−0.40
		6.7d	1.43	1.46		−0.30	−0.36	
		10d	1.40			−0.30		
V	2	5d		1.31	1.26		0.40	0.38
		6.7d		1.30			0.39	
	6	5d		1.03	1.27		−0.13	−0.36
		6.7d		1.02			−0.13	

An asterisk ([*]) marks excessively noisy results.

follows from the component in the direction of motion:

$$0 = (\mathbf{F}_B + \mathbf{F}_D) \cdot (\sin \alpha, 0, \cos \alpha)$$

$$0 = \frac{\pi}{6} d^3 (\rho_L - \rho_G) g \langle \cos \alpha \rangle - \frac{\pi}{8} d^2 \rho_L C_D \langle |\mathbf{v} - \mathbf{u}|(\mathbf{v} - \mathbf{u}) \rangle$$

$$C_D = \frac{4d(\rho_L - \rho_G)g}{3\rho_L \langle |\mathbf{v} - \mathbf{u}|(\mathbf{v} - \mathbf{u}) \rangle} \langle \cos \alpha \rangle = \frac{4d(\rho_L - \rho_G)g}{3\rho_L \langle |\mathbf{v} - \mathbf{u}|(\mathbf{v} - \mathbf{u}) \rangle} \left\langle \frac{v_z - u_z}{|\mathbf{v} - \mathbf{u}|} \right\rangle \tag{21}$$

Secondly, the lift coefficient can be derived from the transverse component of the force balance:

$$0 = (\mathbf{F}_B + \mathbf{F}_L) \cdot (\cos \alpha, 0, -\sin \alpha)$$

$$0 = -\frac{\pi}{6} d^3 (\rho_L - \rho_G) g \langle \sin \alpha \rangle - \frac{\pi}{6} d^3 \rho_L C_L \frac{\partial u_z}{\partial x} \langle |\mathbf{v} - \mathbf{u}| \rangle$$

$$C_L = -\frac{(\rho_L - \rho_G)g}{\rho_L \frac{\partial u_z}{\partial x} \langle |\mathbf{v} - \mathbf{u}| \rangle} \langle \sin \alpha \rangle =$$
$$-\frac{(\rho_L - \rho_G)g}{\rho_L \frac{\partial u_z}{\partial x} \langle |\mathbf{v} - \mathbf{u}| \rangle} \left\langle \frac{v_x}{|\mathbf{v} - \mathbf{u}|} \right\rangle \tag{22}$$

Alternatively, the instantaneous drag and lift coefficient can be averaged, but since the relative velocity ($\mathbf{v} - \mathbf{u}$) hardly fluctuates the difference is very small. This was verified for air bubbles rising in water and the absolute difference in both the drag and lift coefficient was found to be less than 0.008.

5.2. Time-averaging

As an example, the determination of the drag and lift force coefficients from a numerical simulation is shown for an 8 mm air
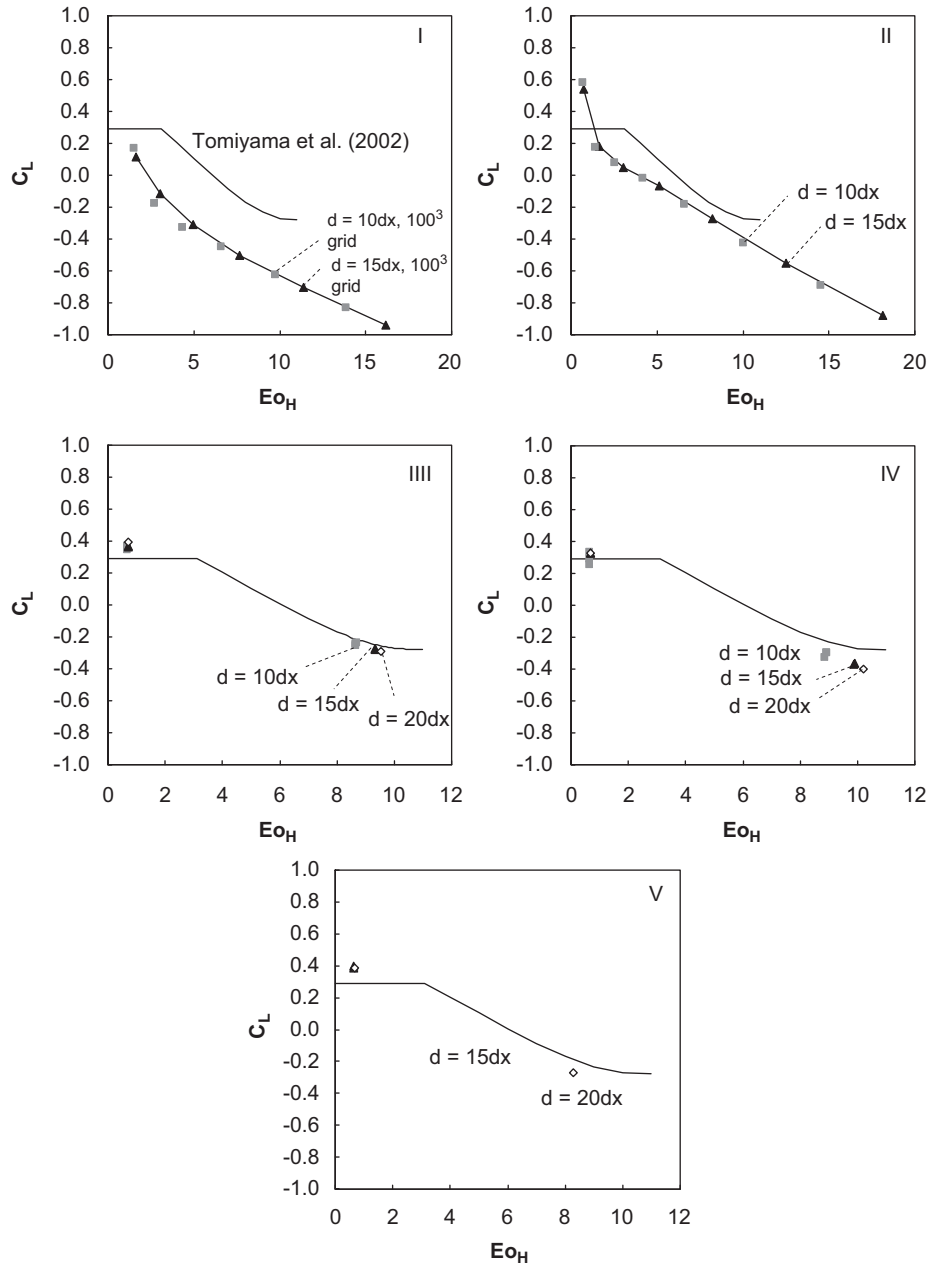

Fig. 8. Numerical lift force coefficients at different grid settings for pure liquids I–V (from left to right). For less viscous liquids (VI–VIII) only the finest grid ($d=20dx$) is used, to limit volume loss and to be able to describe complex shape oscillations. The solid line indicates the prediction by the correlation by Tomiyama et al. (2002).

bubble rising in liquid VI. The instantaneous drag and lift coefficient (Fig. 6) are used to determine the appropriate period for the time-averaging. In this particular case, the bubble takes about 0.7 s to move along a stable helical path, which is responsible for the periodic fluctuations in the drag and lift force. The time-averaging was carried out excluding this initial period. Because the magnitude of the oscillation ($-6 < C_L < 5$) is much larger than the average ($C_L = -0.66$), this interval is adjusted so that the time-averaging starts and stops with the bubble in the same state. Also a sufficient number of oscillation periods was used (typically 5–10), in order to obtain an accurate value.

5.3. Grid dependency

The influence of the domain size and interface resolution is studied by simulating two points (2 and 6 mm bubbles) of each data set using different computational grids (Fig. 7). Legendre and Magnaudet (1998) have shown that the lift force acting on a spherical bubble is very sensitive to wall effects, especially at low Reynolds numbers. For instance, at a Reynolds number of 0.1 they find that a domain size of 50 bubble diameters is still insufficient to completely exclude wall effects. Fortunately, at the same time they conclude that at these conditions the lift force is negligible compared to the drag force, which allows us to shift focus to moderate and low viscosity systems ($Re > 1$). On the other hand, from our experience the complex interface dynamics at higher Reynolds numbers require a higher interface resolution.

First, Table 5 shows that for small bubbles in liquids I and II the drag and lift coefficient vary considerably when the domain size is increased (top to bottom). For less viscous liquids or larger bubbles this effect is significantly smaller because of the higher Reynolds numbers. This is more clearly demonstrated in Fig. 8, showing that the effect of resolution and box size levels off very quickly for larger bubbles. Secondly, it can be observed that the effect of resolution (left to right in Table 5) is quite small, because of the relatively simple interface dynamics and flow profile. Nevertheless, the intermediate resolution ($d = 15\,dx$) is preferred, because it gives considerably less numerical noise and errors related to volume loss. For the three least viscous liquids (VI–VIII) it was found that the highest resolution ($d = 20\,dx$) has to be used to obtain accurate results, because coarser grids give too much errors due to volume loss for the wobbling bubbles to reach a steady state. Also, the bubble shape is more accurately described when using a higher interface resolution.

6. Results

In this section the results of the numerical simulations and the experiments are discussed. The inevitable contaminants due to the shear generation in the experiments strongly affect the results, so that a direct comparison with the 'pure' numerical results is not shown here. Rather, each is treated separately and compared to the available literature data.

6.1. Lift force for bubbles in pure liquids (numerical simulations)

First, the influence of the linear shear field on the drag force and bubble shape is compared to results obtained without a shear field (initially quiescent liquid). As an example, the results for the most viscous and least viscous liquids are shown in Fig. 9. All simulated points have been checked and it can be concluded that there is no influence whatsoever of the shear field on the drag
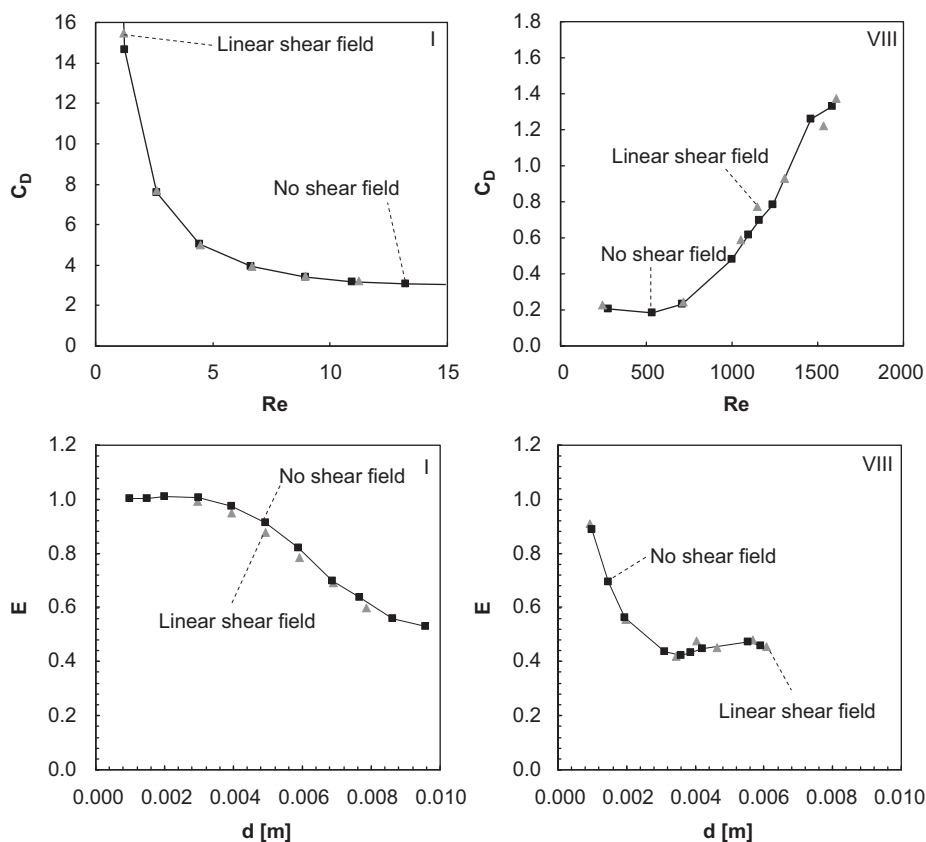

Fig. 9. Numerical drag force coefficient (top) and aspect ratio (bottom) for bubbles in the highest (left) and lowest viscosity pure liquid (right) with and without a linear shear field.

coefficient and bubble aspect ratio, which is not surprising considering the low shear ratio ($Sr < 0.12$) and sufficiently high Reynolds numbers ($Re > 1$) investigated (Adoua et al., 2009). Even when doubling the shear rate, there is still no discernible effect.

Since it is clear that the shear field does not influence the drag force, it is possible to focus on the lift force independently. Fig. 10 shows that for (nearly) spherical bubbles ($E > 0.95$) there is a good agreement with the equation by Legendre and Magnaudet (1998), provided that the liquid is not too viscous. Fortunately, the lift force is relatively unimportant at low Reynolds numbers (Legendre and Magnaudet, 1998) and Eq. (5) works well in this region, so that these differences are not very important. Also, it can be seen that there is a significant difference with the Reynolds-dependant part of the correlation by Tomiyama (Eq. (7), $Eo_H < 4$), which is not surprising as this does not reduce to the analytical solution at neither low nor high Reynolds numbers.

For deformed bubbles the numerical results are first of all plotted versus the inverse bubble aspect ratio (Fig. 11). The theoretical solution for the lift force at infinite Reynolds numbers (Eq. (6)) does not agree at all with the numerical simulations, which can be explained by the fact that the maximum Reynolds number is only 1609. Furthermore, it can be seen that the transition to a negative lift force coefficient for the most viscous liquid (I) already occurs with nearly spherical bubbles, while for less viscous liquids it reaches an apparent limit at $E = 0.45$ because the bubble aspect ratio reaches a limit here (Fig. 9). This interesting phenomenon makes the bubble aspect ratio unsuitable as a parameter for describing the lift force, even though the critical aspect ratio found matches the results by Adoua et al. (2009) in the range $100 < Re < 2000$. Also it neatly demonstrates the inherent superiority of interface tracking methods like 3D front tracking, that calculate the bubble shape as part of the numerical solution, over methods that assume a certain bubble shape.

Secondly, the numerical results are compared to the horizontal Eötvös number-dependant part of the correlation by Tomiyama (Fig. 11, $Eo_H > 4$). The results show that for the most viscous liquid (I) the simulation results are quite different from Tomiyama's

correlation and the other simulation results, which may be related to the low Reynolds numbers. However, more simulations (using a very large domain size) at low Reynolds number have to be conducted in order to investigate this phenomenon further. At similar conditions as Tomiyama used (II–IV) and all the way to the industrially very important water regime (VIII), a good agreement with his correlation is found ($4 < Eo_H < 10.7$), although the lift force is systematically lower in the numerical simulations. The small scatter in the numerical data points is mainly caused by path-instability or wobbling motion of the bubbles, which cause the lift force coefficient to oscillate with very large amplitude (Fig. 6). This makes a very accurate determination of its average
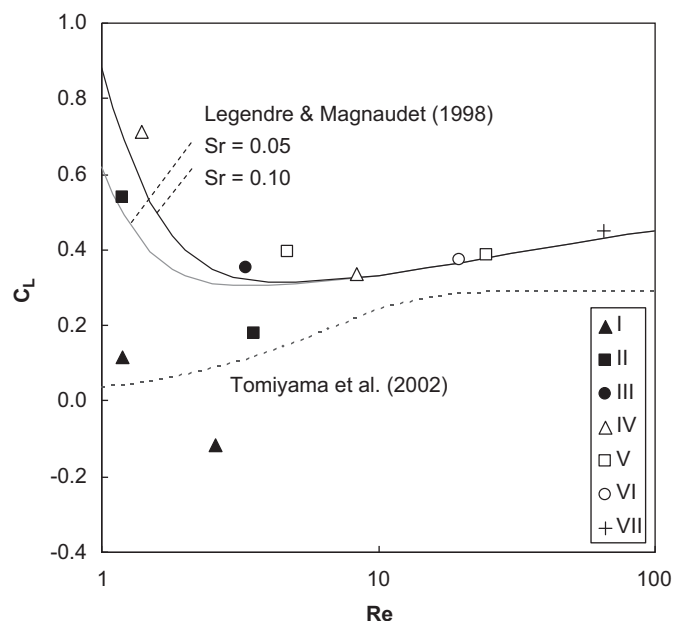

Fig. 10. Numerical lift force coefficient for spherical bubbles ($E > 0.95$) in pure liquids in a linear shear field, showing that the simulations agree well with the correlation by Legendre and Magnaudet (1998) at higher Reynolds numbers.
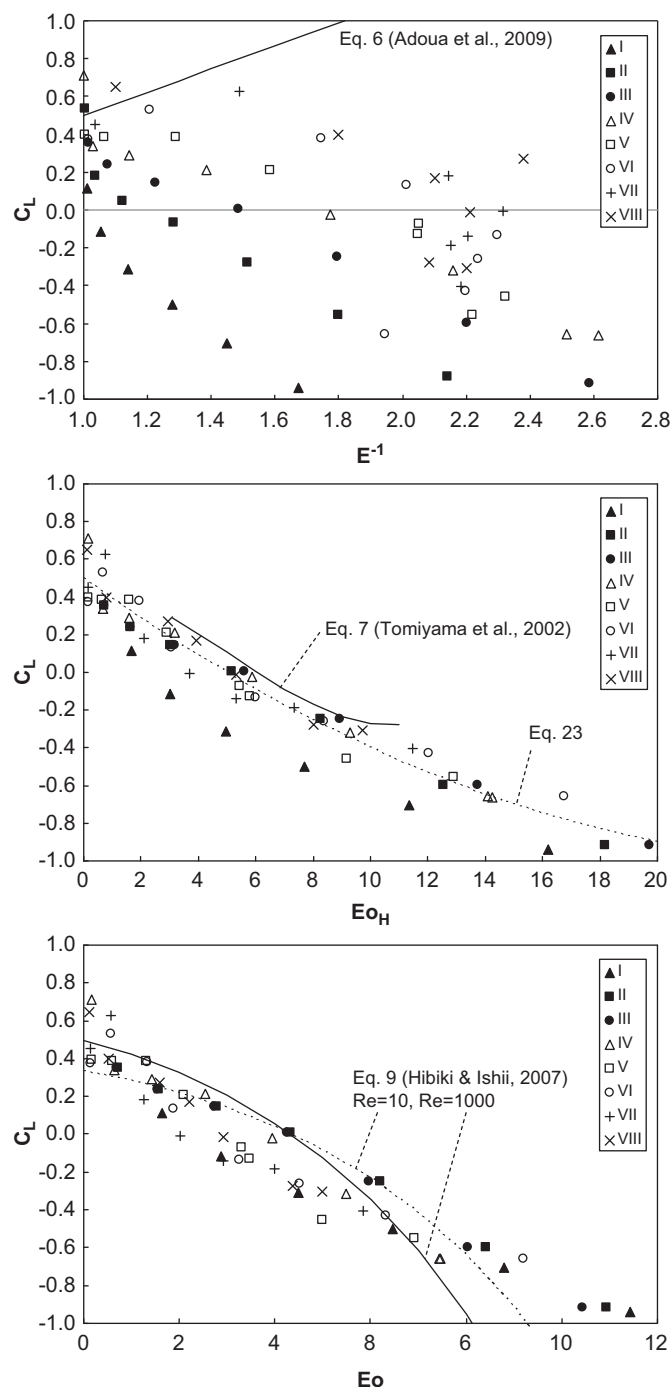

Fig. 11. Numerical lift force coefficient for deformed bubbles in a linear shear field versus inverse bubble aspect ratio and horizontal and regular Eötvös numbers (from top to bottom).
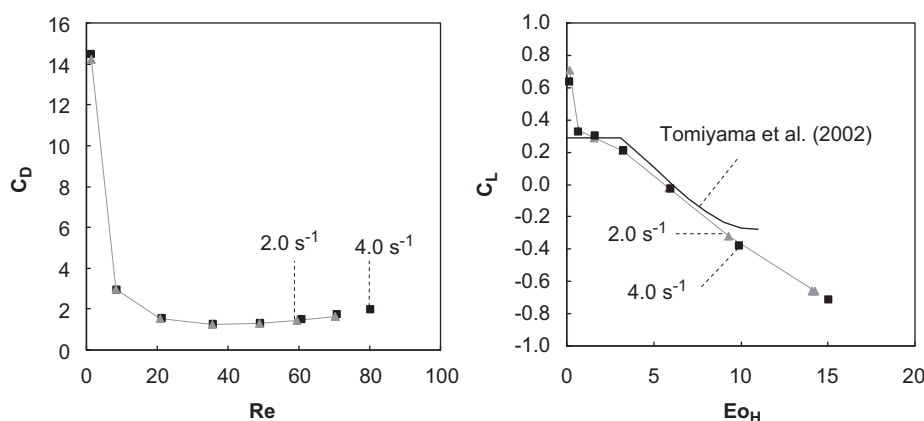
Fig. 12. Numerical influence of the shear rate (2.0 and 4.0 s^{-1}) on the drag and lift force coefficients for bubbles in a moderately viscous pure liquid (IV).

value extremely challenging, moreover because it can take a very long time to reach a steady state. To get rid of the systematic deviation (that was also observed by Bothe et al., 2006), the numerical data (except liquid I) is fitted in a similar way as done by Tomiyama et al. (2002), but making use of the correlation of Legendre and Magnaudet (1998) for spherical bubbles, to obtain a complete correlation:

$$C_L = MIN\left(\sqrt{\left(\frac{6J(Re, Sr)}{\pi^2 \sqrt{Re\,Sr}}\right)^2 + \left(\frac{1}{2}\frac{Re+16}{Re+29}\right)^2},\ 0.5 - 0.11Eo_H + 0.002Eo_H^2\right)$$
(23)

Finally, in Fig. 11 the numerical results are compared to the correlation of Hibiki and Ishii (2007) for two Reynolds numbers (10 and 1000), which approximately match the results of liquids II and VIII respectively. First of all, it can be seen that there is more scatter in the results, when compared to the plot in terms of the horizontal Eötvös number. Secondly, the correlation becomes progressively steeper, where the correlation of Tomiyama and the numerical results predict it should flatten off. Even though the results for spherical bubbles might be good, most industrially relevant cases involve deformed bubbles, so it can be concluded that the correlation by Hibiki and Ishii (Eq. (9)) is not a viable substitute for the popular correlation of Tomiyama (Eq. (7)).

As a final check the effect of increasing the shear rate from 2.0 to 4.0 s^{-1} was determined for bubbles in pure liquids. It was found that there is no influence of the shear rate on the drag and lift force coefficient, except—as predicted by Eq. (5)—at very low Reynolds numbers. As an example, Fig. 12 shows that for liquid IV both the drag and lift force coefficients for both shear rates are very close.

6.2. Lift force for bubbles in contaminated liquids (experiments)

It is well-known that the drag force in experiments can strongly deviate from the results obtained from numerical simulations, because of contaminations affecting the slip conditions at the bubble surface (Fukuta et al., 2008). Fig. 13 shows that this is also the case in the presence of a linear shear field. It can be seen that the linear shear field has no consistent effect on the drag coefficient, meaning that also the lift force for contaminated bubbles can be treated independently from the other forces. There is some scatter in the results—especially for the larger bubbles—because of disturbances during the bubble injection and fluctuations in the linear shear field. Also it was verified that the bubbles had the same aspect ratio as in the case without the linear shear field.
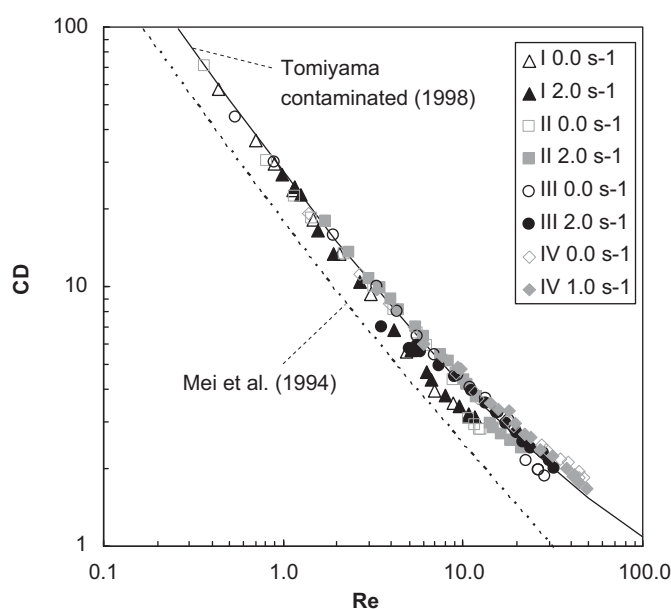

Fig. 13. Experimental drag force coefficient vs. Reynolds number for bubbles in a contaminated liquid. The solid and dashed lines represent the predictions by the correlations by Tomiyama et al. (1998) and Mei et al. (1994) respectively. The experiments show that the drag force is not dependant on the shear rate and also that there is a good agreement with the correlation of Tomiyama et al. (1998).

Secondly, the lift force coefficient can be studied from Fig. 14, at different liquid viscosities and shear rates. Surprisingly, this shows that the shear rate does have an important effect on the lift force coefficient when the liquid is contaminated, which is likely related to the modified shear stress at the bubble surface.

6.3. Wake structure

From literature it was found that large deformed bubbles have a slanted wake structure, which may be a key factor in explaining the negative lift force coefficient. Fig. 15 shows that as soon as the lift coefficient turns negative (6 mm air bubble in liquid II) in the numerical simulations, there is still no (or hardly any) asymmetric wake structure. Only when the bubble diameter is increased to 8 mm, the slanted wake appears. On the other hand, in the experiments (Fig. 16) the slanted wake is already quite pronounced at a bubble diameter of 6 mm in liquid II. These discrepancies are again attributed to the effects of contaminants.
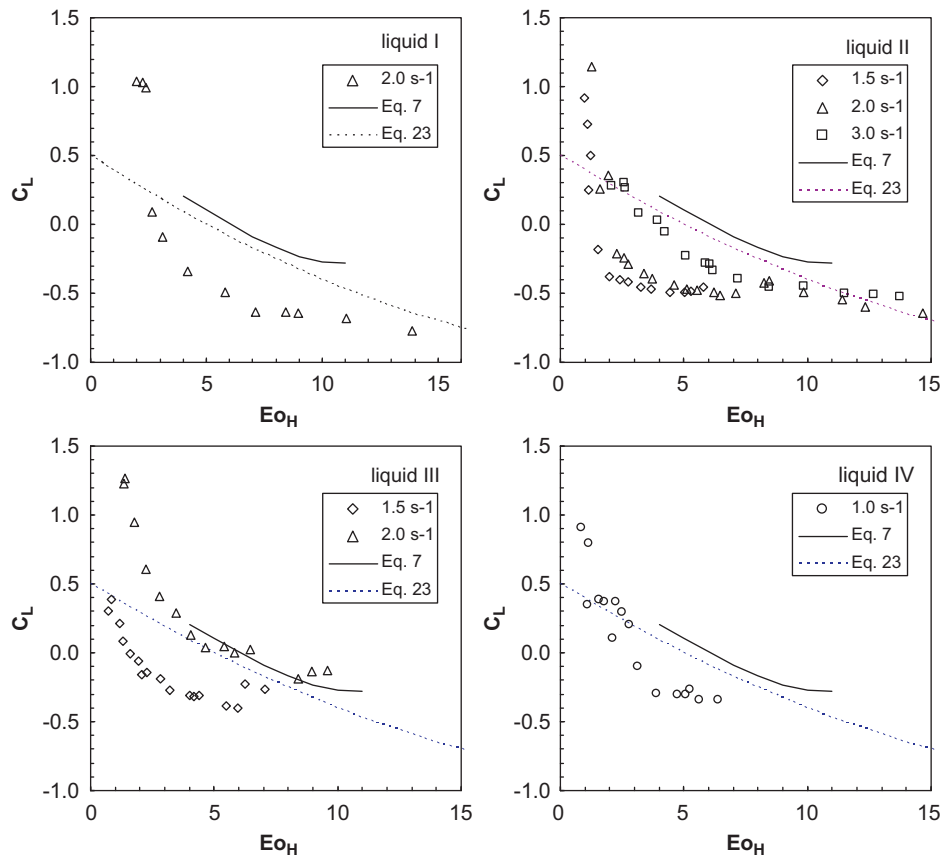
Fig. 14. Experimental lift force coefficient at different shear rates for air bubbles in contaminated liquids (I–IV), showing a strong dependency of the shear rate.
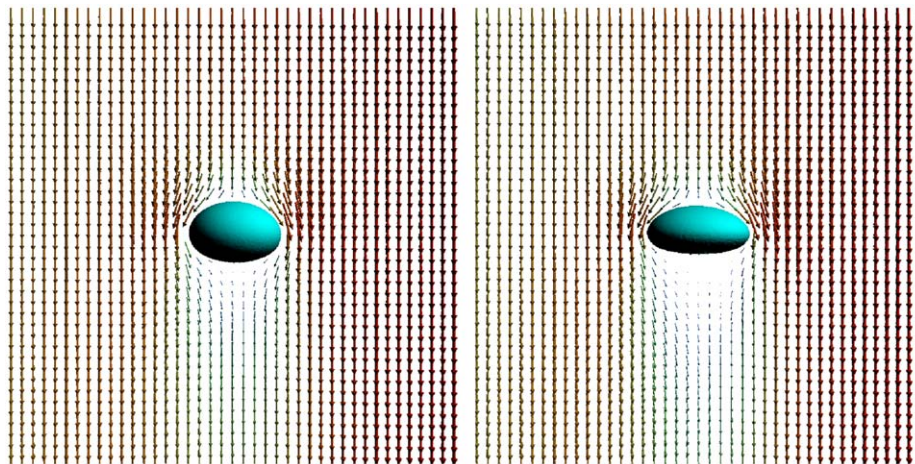

Fig. 15. Flow profile around a 6 mm (left) and 8 mm (right) air bubble in pure liquid II, obtained from the numerical simulations. Both bubbles have a negative lift coefficient, but only the larger bubble has a slanted wake.

7. Conclusions

In this article the lift force has been studied using numerical simulations and experiments, which represent pure and contaminated liquids respectively. The numerical simulations have been carried out at Reynolds numbers above 1, because of the very strong effect of the walls at lower Re numbers, and relatively low dimensionless shear rates $0.008 < Sr < 0.119$. The results show a good agreement with the correlation by Legendre and Magnaudet (1998) for spherical bubbles at sufficiently high Reynolds numbers ($Re > 10$), contradicting the Reynolds-dependant part of Tomiyama's closure (2002, $Eo_H < 4$).

For larger (deformed) bubbles the transition to negative lift force coefficient occurs at similar bubble aspect ratios ($E = 0.45$) as found by Adoua et al. (2009). However, since this coincides with the minimum aspect ratio for large bubbles, it cannot be used to describe when the lift force becomes negative. Secondly, there is a good agreement with the Eötvös-dependant part of the correlation by Tomiyama ($4 < Eo_H < 10.7$), although the lift coefficient was consistently somewhat lower. A correlation was proposed based on a fit of the numerical data for deformed bubbles combined with the correlation of Legendre and Magnaudet (1998) for spherical bubbles. The correlation of Hibiki and Ishii (2007) was also evaluated, but it was discarded due to an asymptotic

Fig. 16. Flow profile around a 6 mm air bubble in contaminated liquid II, obtained using PIV from the experiments. It can be seen that the slanted wake is much more developed than in the numerical simulations.

behaviour contrary to the numerical results and the correlation of Tomiyama. Finally, it was shown that the shear rate has no influence on the drag and lift coefficients.

For the experiments a set-up was constructed consisting of a running belt submerged in a column of liquid. PIV measurements have been used to validate the linearity of the shear field and to calibrate the shear rate. The experimental data ($0.026 < Sr < 0.163$, $1.0 < Re < 49$) show that in a contaminated liquid there is a very strong effect of the shear rate on the lift force and consequently the results are totally different from the numerical simulations and experiments by Tomiyama et al. (2002).

For future research, it is recommended to focus first on the measurement of the type and concentration level of contaminations, because currently there is no clear way of determining the extent of contaminations in the experiments. Once this is clarified, experiments can be done using different levels of contaminations, to study their effect. Also it would be worthwhile to perform some numerical simulations using the same bubble shape as in the front tracking simulations, but now with a rigid surface mimicking contaminated bubbles. This may prove indirectly whether the observed effects can indeed be attributed to contaminants.

Notation

a	amplitude, m
A	cross-sectional area of the bubble, m^2
$\mathbf{A}$	matrix, dimensionless
C	coefficient, dimensionless
Ca	capillary number, dimensionless
d	equivalent bubble diameter, m
d_x, d_y, d_z	distribution functions in one direction, dimensionless
dx, dy, dz	grid size, m
D	volume weighing distribution kernel, dimensionless
$\mathbf{e}_z$	unit vector in the z-direction, dimensionless
E	bubble aspect ratio, dimensionless
E	error, dimensionless
Eo	Eötvös number ($Eo = g(\rho_L - \rho_G)d^2\sigma^{-1}$), dimensionless
Eo_H	horizontal Eötvös number $Eo = g(\rho_L - \rho_G)d_H^2\sigma^{-1}$
$\mathbf{F}$	force, N
F_p	phase fraction, dimensionless
$g, \mathbf{g}$	gravitational constant/acceleration, m s^{-2}
$\mathbf{G}_p$	gradient of the phase fraction, dimensionless
h	height, m
h	mesh width, m
H	Heaviside function, dimensionless
J	function of the Reynolds number and the shear ratio, dimensionless
$\mathbf{k}_i$	location estimates used in the Runge–Kutta time-stepping method, m
La	Laplace number, dimensionless
$M_{i,j}$	second derivate of the spline, m s^{-1}
Mo	Morton number ($Mo = g\eta_L^4(\rho_L - \rho_G)\rho_L^{-2}\sigma^{-3}$), dimensionless
$\mathbf{n}$	unit normal vector, dimensionless
N	number of cells, dimensionless
N_m	number of markers, dimensionless
N_{ph}	number of phases, dimensionless
p	pressure, Pa
Re	Reynolds number ($Re = \rho_L|\mathbf{v} - \mathbf{u}|d\eta_L^{-1}$), dimensionless
s	spline (used for velocity interpolation), m/s
S	surface area, m^2
Sr	shear ratio ($Sr = \omega d|\mathbf{v} - \mathbf{u}|^{-1}$), dimensionless
$\mathbf{t}$	tangent vector, m
t	time, s
$\mathbf{u}$	continuous phase velocity, m s^{-1}
$\mathbf{u}, \mathbf{v}$	correction vectors in the Sherman–Morrison formula, dimensionless
$\mathbf{v}$	bubble velocity, m s^{-1}
V	volume, m^3
w	width, m
x, y, z	Cartesian coordinates, m
$\mathbf{x}$	position, m
$\mathbf{x}$	solution vector, dimensionless
$\mathbf{y}, \mathbf{z}$	solution vectors in the Sherman–Morrison formula, dimensionless

Greek letters

δp	pressure correction, Pa
Δp	pressure jump, Pa
Δt	time step, s
η	dynamic viscosity, Pa s
ρ	density, kg m^{-3}
σ	surface tension coefficient, N m^{-1}
τ	characteristic time, s
ω	shear rate, s^{-1}

Sub-/superscripts

B	buoyancy
d	dispersed phase
D	drag force
f	continuous phase
G	gas phase
h	horizontal direction
i, j, k	grid indices in the x-, y- and z-direction respectively
L	liquid phase, lift force
m	marker

max	maximum
momentum	momentum
n	current time-level
n^*, n^{**}	intermediate time-level
$n+1$	future time-level
p	phase
th	theoretical
v, z	vertical direction
x, y	horizontal directions
0	initial value
σ	surface tension

Acknowledgements

References

Adoua, R., Legendre, D., Magnaudet, J., 2009. Reversal of the lift force on an oblate bubble in a weakly viscous linear shear flow. J. Fluid Mech. 628, 23–41.

Auton, T.R., 1987. The lift force on a spherical body in a rotational flow. J. Fluid Mech. 183, 199–218.

Bagchi, P., Balachandar, S., 2002. Effect of free rotation on the motion of a solid sphere in linear shear flow at moderate Re. Phys. Fluids 14, 2719.

Bothe, D., Schmidtke, M., Warnecke, H.-J., 2006. VOF-simulation of the lift force for single bubbles in a simple shear flow. Chem. Eng. Technol. 29, 1048–1053.

Centrella, J., Wilson, J., 1984. Planar numerical cosmology. II. The difference equations and numerical tests. Astrophys. J. Suppl. Ser. 54, 229.

Clift, R., Grace, J.R., Weber, M.E., 1978. Bubble, Drops and Particles. Academic Press, New York.

Dijkhuizen, W., Roghair, I, van Sint Annaland, M., Kuipers, J.A.M., 2009. DNS of gas bubbles behaviour using an improved 3D front tracking model—model development. Chem. Eng. Sci., Submitted for publication.

Deen, N.G., van Sint Annaland, M., Kuipers, J.A.M., 2004. Multi-scale modeling of dispersed gas–liquid two-phase flow. Chem. Eng. Sci. 59, 1853–1861.

Fukuta, M., Takagi, S., Matsumoto, Y., 2008. Numerical study on the shear-induced lift force acting on a spherical bubble in aqueous surfactant solutions. Phys. Fl. 20.

Hibiki, T., Ishii, M., 2007. Lift force in bubbly flow systems. Chem. Eng. Sci. 62, 6457–6474.

Kurose, R., Komori, S., 1999. Drag and lift forces on a rotating sphere in a linear shear flow. J. Fluid Mech. 384, 183.

Legendre, D., Magnaudet, J., 1997. A note on the lift force on a spherical bubble or drop in a low-Reynolds-number shear flow. Phys. Fluids 9, 3572–3574.

Legendre, D., Magnaudet, J., 1998. The lift force on a spherical bubble in a viscous linear shear flow. J. Fluid Mech. 368, 81–126.

McLaughlin, J.B., 1991. Inertial migration of a small sphere in linear shear flows. J. Fl. Mech. 224, 261–274.

Mei, R., Lawrence, C.J., Klausner, J.F., 1994. A note on the history force on a spherical bubble at finite Reynolds number. Phys. Fl. 6, 418–420.

Mei, R., Klausner, J.F., 1994. Shear lift force on spherical bubbles. Int. J. Heat Fluid Flow 15, 62–65.

Naciri, M.A., 1992. Contribution à l'etude des forces exercées par un liquide sur une bulle de gaz: portance, masse ajouté. Ph.D. Thesis, L'école Centrale de Lyon, France.

Palaparthi, R., Papageorgiou, D.T., Maldarelli, C., 2005. Theory and experiments on the stagnant cap regime in the motion of spherical surfactant-laden bubbles. J. Fl. Mech. 559, 1–44.

Popinet, S., Zaleski, S., 1999. A front-tracking algorithm for the accurate representation of surface tension. Int. J. Numer. Methods Fluids 30, 775.

Prosperetti, A., Navier–Stokes numerical algorithms for free-surface flow computations: an overview, Drop-Surface Interaction, p. 237, 2002.

Saffman, P.G., 1965. The lift on a small sphere in a slow shear flow. J. Fluid Mech. 22, 385–400.

Scardovelli, R., Zaleski, S., 1999. Direct numerical simulation of free-surface and interfacial flow. Annu. Rev. Fluid Mech. 31, 567.

Singh, R., Shyy, W., 2007. Three-dimensional adaptive Cartesian grid method with conservative, interface restructuring and reconstruction. J. Comput. Phys. 224, 150–167.

van Sint Annaland, M., Deen, N.G., Kuipers, J.A.M., 2003. Multi-level modeling of dispersed gas–liquid two-phase flows, series: heat and mass transfer. In: Sommerfeld, M, Mewes, D. (Eds.), Springer, Berlin.

van Sint Annaland, M., Dijkhuizen, W., Deen, N.G., Kuipers, J.A.M., 2006. Numerical simulation of gas bubbles behaviour using a 3D front tracking method. A.I.Ch.E. J. 52, 99.

de Sousa, F.S., Mangiavacchi, N., Nonato, L.G., Castelo, A., Tomé, M.F., Ferreira, V.G., Cuminato, J.A., McKee, S., 2004. A front-tracking/front-capturing method for the simulation of 3D multi-fluid flows with free surfaces. J. Comput. Phys. 198, 469.

Tomiyama, A., Kataoka, I., Zun, I., Sakaguchi, T., 1998. Drag coefficients of single air bubbles under normal and micro gravity conditions. JSME Int. J. Ser. B 41, 472–479.

Tomiyama, A., Tamai, H., Zun, I., Hosokawa, S., 2002. Transverse migration of single bubbles in simple shear flows. Chem. Eng. Sci. 57, 1849–1858.

Tryggvason, G., Bunner, B., Esmaeeli, A., Juric, D., Al-Rawahi, N., Tauber, W., Han, J., Nas, S., Jan, Y.-J., 2001. A front-tracking method for the computations of multiphase flows. J. Comput. Phys. 169, 708.

Unverdi, S.O., Tryggvason, G., 1992. A front tracking method for viscous, incompressible, multi-fluid flows. J. Comput. Phys. 100, 25.

Zaleski, S., 2005. Interface tracking—VOF, VKI lecture series, Von Karman Institute for Fluid Mechanics, Belgium.